Matching silicon-based anodes with sulfide-based solid-state electrolytes for Li-ion batteries

Martine Grandjean, Mélanie Pichardo, Yohan Biecher, Cédric Haon, Pascale Chenevier

To cite this version:

Martine Grandjean, Mélanie Pichardo, Yohan Biecher, Cédric Haon, Pascale Chenevier. Matching silicon-based anodes with sulfide-based solid-state electrolytes for Li-ion batteries. Journal of Power Sources, 2023, 580, pp.233386. 10.1016/j.jpowsour.2023.233386 . cea-04153304

HAL Id: cea-04153304
https://cea.hal.science/cea-04153304v1

Submitted on 6 Jul 2023

Matching Silicon-based anodes with solid-state electrolytes for Li-ion batteries

Martine Grandjean,[1,2] Mélanie Pichardo,[1,2] Yohan Biecher,[2] Cédric Haon,[2] Pascale Chenevier [1]

[1] Univ. Grenoble Alpes, CEA, CNRS, IRIG, SYMMES, 38000 Grenoble, France
[2] Univ. Grenoble Alpes, CEA, LITEN, DEHT, 38000 Grenoble, France

Highlights

- Comparison of two sulfide-based solid electrolytes $Li_{10}SnP_2S_{12}$ and Li_6PS_5Cl showing different reactivity with silicon anode
- Formation of a thinner SEI during cycling for Si nanowires demonstrated by impedance spectroscopy
- Due to their size and morphology, silicon nanowires are more suitable for efficient cycling in all-solid-state batteries than micron-sized silicon particles.

Abstract

Thanks to their high ionic conductivity and appropriate mechanical properties, sulfide-based solid electrolytes (SSE) are increasingly studied for a use in all-solid-state batteries (ASSBs). Silicon is abundant, non toxic and has a high theoretical capacity, and therefore is a promising active material in ASSBs. We first study the compatibility between two different solid electrolytes with similar ionic conductivity, $Li_{10}SnP_2S_{12}$ (LSnPS) and Li_6PS_5Cl (LPSCl), and micron-sized silicon based anode. LPSCl appears to be less reactive than LSnPS and it is then used to determine the most appropriate silicon size and shape for efficient cycling. Two silicon materials are compared, micron-sized silicon particles (µSi) and silicon nanowires (SiNWs). Energy Dispersive X-ray spectroscopy (EDX) mapping of the composite powders shows a better dispersion of the SiNWs in the LPSCl matrix. Galvanostatic cycling and Electrochemical Impedance Spectroscopy (EIS) measurements highlight the greater compatibility of SiNWs compared to µSi in ASSBs with a high specific delithiation capacity of 2600 mAh/g_{Si} at the first cycle, while limiting the polarization and maintaining a relatively stable lithiation mechanism during cycling.

Keywords

All-solid-state batteries, sulfide solid electrolyte, silicon anode, silicon nanowires

1. Introduction

All-solid-state batteries (ASSBs) are considered as one of the promising next-generation rechargeable battery system thanks to their high energy density and enhanced safety[1–4]. Sulfide-based solid electrolytes (SSE) have shown great potential due to their high ionic conductivity and appropriate mechanical properties[5,6]. According to their structures, SSE can be classified into three categories[7]: (i) thio-LISICON as xLi_2S-$(1-x)P_2S_5$ [8] showing an ionic conductivity of about 0.1 mS/cm, (ii) $Li_{11-x}M_{2-x}P_{1+x}S_{12}$ (M = Ge, Si, Sn,..) such as $Li_{10}SnP_2S_{12}$[9] with an ionic conductivity of 4 mS/cm and (iii) lithium argyrodite Li_6PS_5X (X = Cl, Br, I) reaching an ionic conductivity of 1 mS/cm for Li_6PS_5Cl[10]. ASSBs have brought high hopes expecting that they would perform well with lithium metal anodes. However, lithium plating happens also along solid electrolyte grain boundaries, ensuing short-circuits[11–15]. We thus turn to silicon (Si) as a safer and light-weight anode design for ASSBs[16]. Early investigations have demonstrated the high capacity of silicon in solid state microbatteries[17–21]. But the strong volume expansion of silicon limits the thickness of Si thin film anodes to less than 100 nm, so that only a very low areal capacity can be reached. Nanostructuring silicon proved efficient to prevent the detrimental effects of Si swelling in standard lithium-ion batteries[22,23], and a few papers report encouraging results in ASSBs[24]. Trevey *et al.* compared the electrochemical performances of silicon nanoparticles (SiNPs) and micron-size silicon in SSE[25]. They showed that SiNPs improve the cycling stability as well as the capacity of the cell. To further improve Si-based ASSBs, Okuno *et al.* synthesized nanoporous SiNPs[26]. The volume expansion of the SiNPs is buffered by the shrinkage of the nanopores, and the elasticity of the SSE accomodates the strain due to this expansion. The nanoporous SiNPs achieve a retention of 80% of the initial capacity at the 150th cycle, whereas the non-porous micron-size silicon particles reach only 19%. In liquid electrolytes, silicon nanowires (SiNWs) also proved to prevent silicon cracking[27–31]. However, to the best of our knowledge, no studies have used SiNWs as active material for ASSBs.

In the present study, we investigate the compatibility of solid electrolytes with silicon anodes, and the most appropriate silicon size and shape for efficient cycling in ASSBs of high capacity. As silicon is highly reactive to oxygen at high temperature[32] and undergoes sintering[33] as low as 400°C, cold pressing-compatible sulfide solid electrolytes were preferred for silicon-based ASSBsin this study. We thus compare two SSEs with close ionic conductivity, $Li_{10}SnP_2S_{12}$ (LSnPS) and Li_6PS_5Cl (LPSCl), facing two types of silicon as the anode active material, a micron-sized powder (µSi) and SiNWs.

2. Materials & Methods

Materials. $Li_{10}SnP_2S_{12}$ (LSnPS) and Li_6PS_5Cl (LPSCl) were purchased from NEI, USA. Micron-sized silicon particles (µSi) were purchased from Elkem, Norway. Lithium and indium foils were purchased from Sigma Aldrich, France. Diphenylsilane was purchased from Chemical Point, Germany.

SiNW synthesis. SiNWs were synthesized in the laboratory as previously described[31,32]. Briefly, a NaCl powder covered with gold colloids as growth catalysts is enclosed with diphenylsilane in a pressure reactor under vacuum, and heated to 430°C for 4 h. After cooling down, the pressure is carefully released and the SiNWs are recovered by washing away the organic by-products in acetone and dichloromethane, and by dissolving the NaCl sacrificial support in water. The SiNWs grown by this method contain gold and have a native passivation layer of phenyls at their surface.

Material characterisation. Scanning Electron Microscopy (SEM) was operated on an Ultra 55+ (Zeiss, Germany) microscope at an accelerating voltage of 5 kV and working distance of 5 mm. For the quantitative Energy Dispersive X-ray spectroscopy (EDX), 2 mg of composite were pressed into a 5 mm-diameter pellet in a hydraulic press (Specac, UK) under 2 tons of pressure for 2 minutes, to obtain a dense sample (> 85%) with a flat surface, to allow for a quantitative analysis. For the EDX mapping, a small amount of composite powder is applied to a carbon tape and the excess is removed. This step is carried out in a glove box and an airtight box is used to introduce the samples into the SEM. Energy Dispersive X-ray spectroscopy spectra were recorded on a Zeiss Ultra 55+ microscope at an accelerating voltage of 10 kV at working distance of 7 mm. The apparatus was first calibrated with a series of elemental standards (Zeiss). The Brunauer, Emmet and Teller (BET) method was used to measure the SBET specific surface of the different samples using a 120 Micromeritic apparatus (Tristar II and Flowsorb 2300).

Electrochemical characterisation. All electrochemical characterisations were performed in half-cell configuration. The working electrode corresponds to the silicon composite electrode, and the counter-electrode is a lithium-indium (Li-In) alloy. The use of this alloy limits the possible formation of secondary products such as Li_3P or Li_2S when Li metal comes into contact with sulfides, while limiting the appearance of dendrites[13,34]. Moreover, the Li-In alloy has the advantage of having a constant redox potential at 0.6 V vs Li^+/Li for a lithium molar composition of between 5 and 45%[35]. Thus all the potentials reported in this paper are expressed vs. $Li^+/LiIn$. The composite electrode consists of 30 wt% active material, 20 wt% conductive additive (VGCF) and 50 wt% solid electrolyte. The different powders are mixed in a mortar for about 15 min and then stored in a glove box. The cells are manufactured in a fixed volume mould of 7 mm diameter which can be pressurised by its screws using a press. The advantage of this cell is that the assembly is prepared inside and the measurements are made directly in the system. The manufacturing protocol is shown in Figure S1. Briefly, 35 mg of pure electrolyte was pressed at 255 MPa, then 3 mg of a composite powder was pressed upon the first pellet with a stainless steel current collector (30µm). On the other side, a piece of Li-In alloy (38 mol% of Li and 62 mol% of In) was finally added as the counter electrode (with a large excess of capacity) and reference electrode with a stainless steel current collector (30µm), and the whole cell was pressed to 127 MPa before cycling. The average composite electrode thickness is 63 µm for the µSi composite and 78 µm for the SiNWs composite (respective apparent electrode density 1.2 and 1.0 g/cm^3 and compacity 65% and 52%). The average thickness is 625 µm for the solid electrolyte. The thicknesses of the composite electrodes and the electrolyte pellet were measured with a Mitutoyo micrometer after densification of the powder at 255 MPa for 5 min. The electrochemical tests were carried out with Biologic (France) potentiostat at room temperature. Galvanostatic cycling limited in potential between -0.6 and 1 V were carried out at a cycling rate of C/20 with a program of constant current, except for a floating step at constant voltage at the end of lithiation. For the electrochemical impedance spectroscopy (EIS) measurement, an applied voltage of 10 mV over a frequency range from 1 MHz to 100 mHz was used. The impedance measurements were recorded before cycling and at the end of each lithiation and each delithiation. The results of EIS measurements are plotted in the Nyquist representation and by multiplying the Ohm measurement by the form factor (area of the composite electrode divided by its thickness) to compare the two silicon materials despite their different thicknesses.

3. Results & Discussion

3.1. Testing stability of sulfide solid electrolytes towards Silicon

$Li_{10}SnP_2S_{12}$ (LSnPS) and Li_6PS_5Cl (LPSCl) were chosen for their high ionic conductivity of $1.4.10^{-3}$ S/cm and $1.7.10^{-3}$ S/cm respectively at room temperature (Fig. S2), and for their commercial availability. Fig. S2 and S3 present SEM images of these electrolytes and ionic conductivity measurements of pure solid electrolyte pellets. The two electrolytes were evaluated in half-cell configuration with µSi as the anode active material and a Li-In alloy counter electrode.

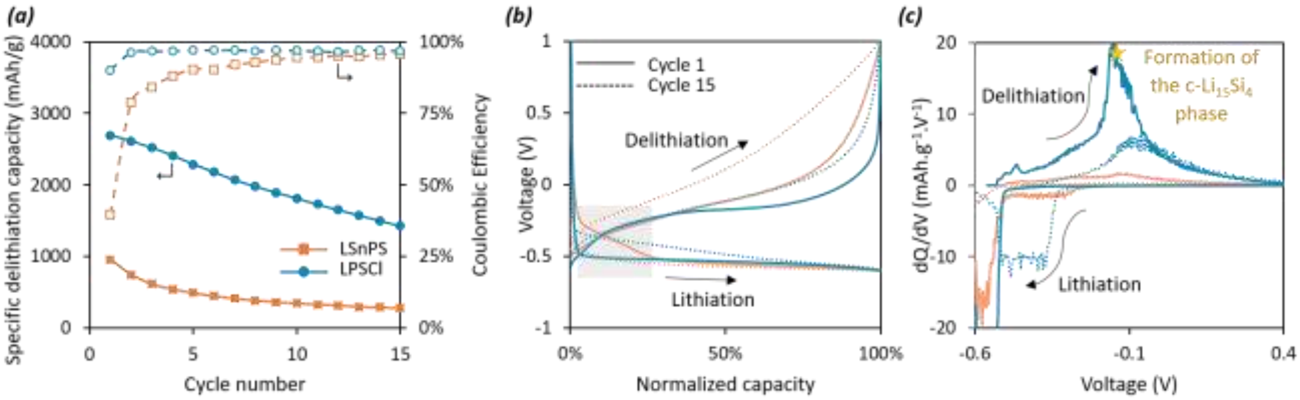

<u>Figure 1.</u> (a) Specific delithiation capacity in full dots and Coulombic efficiency in empty dots of µSi/LPSCl/Li-In (blue) and µSi/LSnPS/Li-In (orange) cells as a function of the number of cycles. (b) Normalized galvanostatic curves at the 1st and 15th cycle for µSi/LPSCl/Li-In and µSi/LSnPS/Li-In cells. (c) dQ/dV curves at the 1st and 15th cycle for µSi/LPSCl/Li-In and µSi/LSnPS/Li-In cells.

Figure 1 shows the electrochemical performances of cells built from µSi and LSnPS or LPSCl, denoted in the following LSnPS-cell and LPSCl-cell respectively. A striking difference shows up on the specific capacity (Fig. 1a). LPSCl-cells show a reversible capacity above 2500 mAh/g at the first cycle while the LSnPS-cell capacity is below 1000 mAh/g and loses 50% after only 5 cycles (490 mAh/g_{Si}). Accordingly, the initial Coulombic efficiency is 40% for LSnPS-cell versus 90% for LPSCl-cell. At the 2nd cycle, the Coulombic efficiency (CE) reaches 97% for the LPSCl-cells. These data suggest a higher reactivity of LSnPS towards silicon, confirmed in the normalized galvanostatic curves: the additional shoulder (in the grey shaded area on Fig. 1b) during the first discharge of LSnPS-cells at -0.25 V denotes an irreversible electrochemical reaction, probably the solid-electrolyte interphase (SEI) formation. At the 15th cycle, in delithiation, LSnPS-cells require a 0.15 V higher voltage to attain 35% capacity than LPSCl-cells. This polarization shows the appearance of a bigger internal resistance during cycling for LSnPS-cells. Finally, the derivative dQ/dV curves (Fig. 1c) for LPSCl-cell reveals the formation of the crystalline $Li_{15}Si_4$ (c-$Li_{15}Si_4$) phase. Indeed, the strong peak (labelled by a yellow star) at -0.15 V vs Li^+/LiIn in delithiation is characteristic of the biphasic delithiation of c-$Li_{15}Si_4$, absent in the LSnPS-cell dQ/dV profile. This denotes a deep silicon lithiation only with the LPSCl electrolyte.

Thus, although having very similar ionic conductivities, these two electrolytes show a different reactivity in silicon-containing anodes. The LSnPS electrolyte shows a much higher reactivity with micron-sized silicon particles than LPSCl which results in a much faster degradation of performance. LPSCl is thus selected for the rest of the study.

3.2. Looking for the most appropriate shape and size for Silicon

LPSCl was then tested in the same half-cell configuration with either µSi or SiNWs as the active material, denoted µSi-cell and SiNW-cell respectively. We first investigated about the quality of mixing in the composite of SSE, carbon fibers and active material before pressing by electron microscopy and elemental mapping. The LPSCl powder has a typical size of 1-10 µm (Fig. S2), and VGCF fibers are about 10 µm in length.

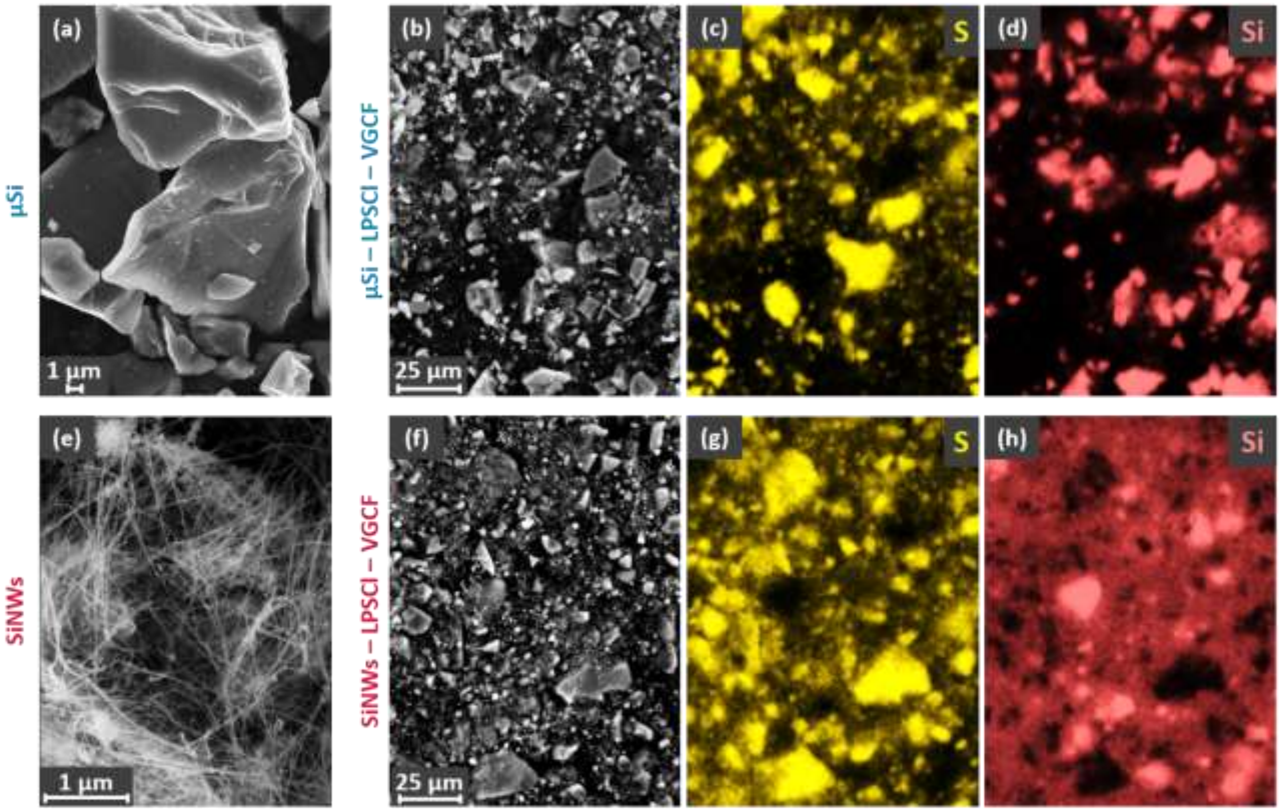

Figure 2: SEM images of pure µSi (a) and SiNWs (e); SEM images (b,f) and corresponding EDX mapping of elements S (c,g) and Si (d,h) for µSi-LPSCl-VGCF (b,c,d) and SiNW-LPSCl-VGCF (f,g,h) composites.

Figure 2a and 2e show the structure of the two studied silicon materials. µSi is a ground powder of metallurgic silicon with a typical size of 2-10 µm. SiNWs have a diameter of 10 nm and a few µm in length, and gather in 1-10 µm sized agglomerates[31]. Their elemental composition is Si/C/O/Au = 86/9/3/2 wt% as measured by quantitative EDX, and the specific area measured by the BET method is 230 m^2/g[32]. These two materials are therefore different in morphology and porosity.

In the EDX mapping, the distribution of the electrolyte in the composite powder can be tracked through the S-element map (Fig.2c and 2g) while the distribution of the active material can be seen through the Si-element map (Fig. 2d and 2h). The expected 1-10 µm silicon particles or agglomerates are clearly visible in both composites. However, in the µSi-LPSCl-VGCF composite, the Si and S maps appear as mutually exclusive, as expected from the mixture of dense microparticles, while the SiNW-LPSCl-VGCF composite is mixed much more finely. Indeed, part of the SiNWs appear to distribute widely in the composite between the agglomerates. The LPSCl distribution is also more homogeneous in the SiNW-LPSCl-VGCF composites, but the solid electrolyte does not penetrate inside the SiNW-agglomerates.

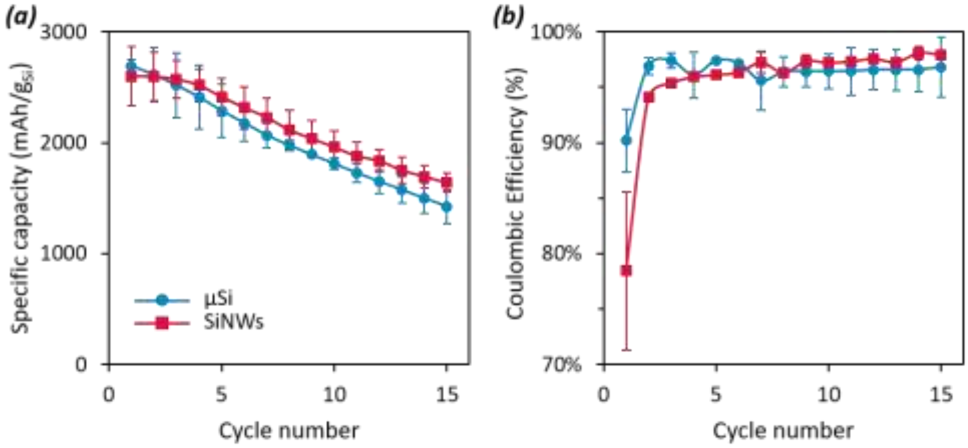

<u>Figure 3:</u> (a) Specific delithiation capacity and (b) CE of SiNW-cells (squares) and µSi-cells (dots) as a function of the number of cycles and at a cycling rate of C/20. Data are averaged over at least 3 cells.

Electrochemical characterization was then performed on µSi- and SiNW-cells (Fig. 3). Despite their very different morphologies, µSi-cells and SiNWs-cells show close cycling performances. At the first cycle, the specific capacity of µSi-cells reach 2700 mAh/g_{Si} vs 2600 mAh/g_{Si} for SiNW-cells (Fig 3a), which represents about 75% of the expected capacity of Si. After 15 cycles, the specific capacity reaches 1400 mAh/g_{Si} and 1630 mAh/g_{Si} corresponding to a capacity retention of 53% and 63% for µSi- and SiNW-cells respectively. Thus, the cycling stability of SiNW anodes is slightly better. The initial CE (Fig 3b) is lower for SiNW-cells (78%) than for µSi-cells (90%). Such difference is expected since the specific area of SiNWs (230 m^2/g) is much higher than that of µSi (1 m^2/g). The effect of specific area on the initial CE is well documented in liquid-electrolyte lithium batteries[31,36]. The loss in capacity after the first cycle is indeed due to the irreversible formation of SEI, the amount of which is proportional to the area of active material exposed to the electrolyte[31]. The initial CE obtained with µSi-cells is consistent with that obtained in liquid electrolyte, whereas for SiNWs of the same diameter, the first CE is much lower in liquid electrolyte (65%)[31]. From our previous results, a first CE of 78% in liquid electrolyte would be expected from SiNWs with a specific surface area around 100 m^2/g [31]. Indeed, even with the good dispersion observed in the SiNW-based anode (Fig. 2h), only part of the SiNW surface is in contact with the SSE since the SSE does not penetrate inside the SiNW agglomerates. The CE at the 15th cycle attains 98% and 96% for SiNW- and µSi-cells respectively, showing a slightly better performance for SiNWs.

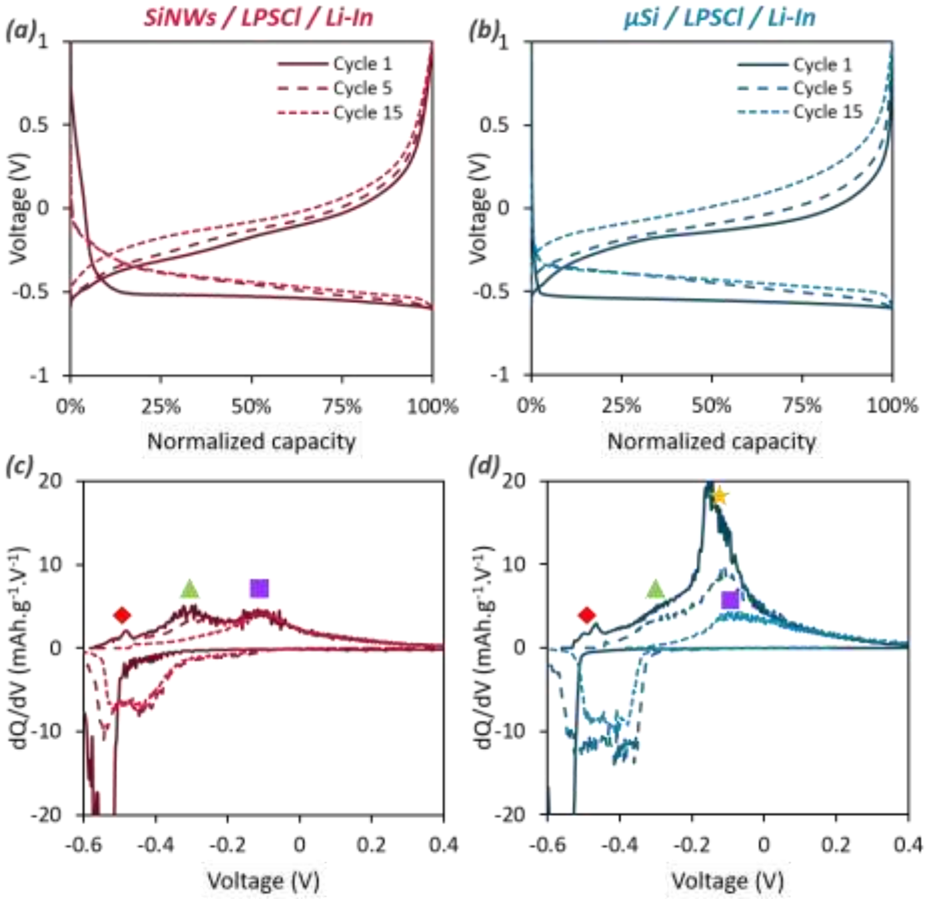

<u>Figure 4:</u> Normalized galvanostatic curves (a,b) and dQ/dV derivatives (c,d) at the 1st, 5th and 15th cycle for SiNW-cells (a,c) and µSi-cells (b,d).

To confirm this, a more detailed study of the normalized galvanostatic curves and their dQ/dV derivatives was carried out (Fig. 4). The galvanostatic curves exhibit a greater polarization for µSi- than SiNW-cells. Indeed, at the 15th cycle, µSi-cells requires a 0.1 V higher voltage in delithiation to attain 35% capacity than SiNW-cells. This indicates the appearance of a higher internal resistance during cycling for µSi-cells.

The dQ/dV curves reveal differences between the two materials in the delithiation-lithiation mechanism. As expected, for both materials, the first lithiation results in a sharp peak around -0.52 V, characteristic of the lithiation of crystalline Si. Subsequent lithiations give rise to the two expected peaks at -0.35 and -0.5 V, typical of the lithiation of amorphous Si. The major differences appear in delithiation, where the expected characteristic peaks (Fig. 4c-d) are due to the VGCF delithiation at -0.48 V (pointed by a diamond), and to the delithiation of silicon at -0.3 V (triangle), -0.15 V (star) and -0.1V (square). The presence of one or two peaks in silicon delithiation depends on the phase obtained at the end of lithiation, either c-$Li_{15}Si_4$ or an amorphous Li_xSi phase. The presence of two peaks at -0.3 and -0.1 V corresponds to the successive delithiation of amorphous lithiated silicon into the two intermediate alloys $Li_{2.3}Si$ and $Li_{1.7}Si$. Alternatively, the presence of one single peak corresponds to the delithiation of c-$Li_{15}Si_4$ into the amorphous Li_2Si phase. This peak at -0.15 V is sharpest because it corresponds to a biphasic reaction, while the -0.3 and -0.1 V peaks relate to more progressive mechanisms. If lithiation is partial, only the -0.1 V peak is observed. The delithiation into amorphous Si gets complete at 0.4 V[37].

For the SiNW-cells, the first delithiation shows the two peaks at -0.3 and -0.1 V, indicating the presence of amorphous Li_xSi at the end of lithiation. On the contrary, for the µSi-cells, the single -0.15 V peak is observed, indicating the formation of c-$Li_{15}Si_4$. Thus, for a part of the silicon particles, µSi-cells attain a deeper first lithiation than SiNW-cells. Indeed, the formation of c-$Li_{15}Si_4$ is disfavoured in nano-sized silicon[31], even when the maximum capacity is nearly attained. At the 5th cycle, the delithiation peaks are almost identical to those of the 1st cycle for SiNW-cells, showing a good stability of the lithiation mechanism. By contrast, a sharp change in lithiation mechanism shows up as soon as the 2nd cycle for the µSi-cells (Fig. S4), as the -0.3 V peak appears, showing that c-$Li_{15}Si_4$ phase is no longer predominant. At the 15th cycle, only the peak at -0.1 V is still visible for both materials, indicating a reduced level of lithiation consistent with the capacity loss.

SiNWs as active material thus provide a high capacity and limit the polarization during cycling, while maintaining a relatively stable lithiation mechanism over 15 cycles. On the contrary, although showing a slightly higher first reversible capacity as well as deeper lithiation, µSi results in a higher degradation of the electrode.

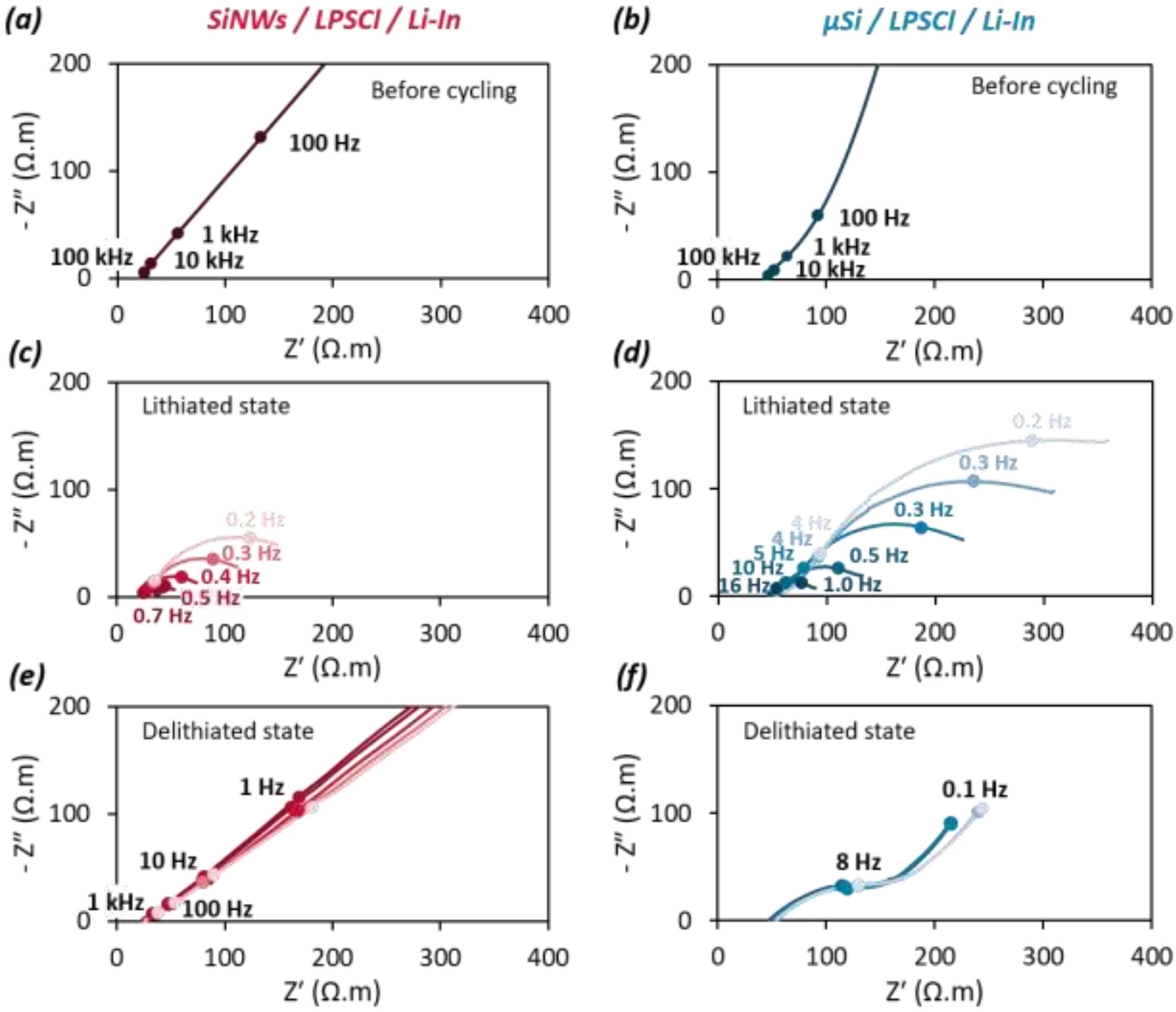

Figure 5: Electrochemical impedance spectroscopy before (a, b) and during cycling at C/20 at the end of silicon lithiation (c, d) and delithiation (e, f) of the 1st, 2nd, 5th, 10th and 15th cycles (scaled from dark to light color) for (a, c, e) SiNWs/LPSCl/Li-In and (b, d, f) µSi/LPSCl/Li-In cells. The frequencies plotted on (c,d,f) are inflection points of the corresponding Bode diagrams (Fig. S5c-f).

To complete this study, we used electrochemical impedance spectroscopy analyses in the Nyquist (Fig. 5) and Bode (Fig. S5) plots. Impedance measurements were recorded in symmetrical configuration at the pristine state and during cycling in half-cell configuration in the lithiated and delithiated state.

The resistance at very high frequency is generally due to the SSE resistance R_e[38]. Here, SiNW-cells present a significantly lower R_e of 20 Ω.m as compared to µSi-cells (45 Ω.m). These resistances do not change significantly during cycling, showing that the SSE does not lose its ion conduction properties. A lower R_e for SiNW-cells might sound surprising, as one would expect that SiNWs finely dispersed in the SSE (as observed in the EDX mapping in Fig. 2h) could disturb the sintering of argyrodite, multiply the grain boundaries and thus reduce its overall ionic conductivity. Apparently, this does not happen. To the contrary, it seems that the intimate composite of SiNWs and SSE offers wider and/or shorter ion conduction paths in the electrode than the µSi-SSE mixture, in which the larger and non-porous µSi particles reduce the volume available to electrolyte percolation.

EIS measurements in the pristine state are reproducible, both in symmetrical (Fig. 5ab and Fig. S5ab) and half-cell configuration (Fig. S6ab). Compared to the Si composite electrodes, the small contribution of the Li-In electrode (Fig. S5b) can be neglected, as was previously reported[5]. Changes in the cell impedance are therefore attributed to phenomena within the composite electrode. In the pristine state, EIS does not reveal the characteristic half circle of an RC circuit. Indeed, for non-lithiated silicon, the variation of chemical potential of Li^+ with lithium concentration is very strong as shown on the galvanostatic curves (Fig. 4ab). In such case, a charge transfer phenomenon does not appear as an RC circuit[39,40]. A clear difference between the two silicon materials shows up already in the pristine state. For SiNW-cells, diffusion is limiting as shown by the 45° slope in the Nyquist profile. For µSi-cells, the range where diffusion is limiting is smaller (1 - 100 kHz) and, at low frequency, a capacitive limitation is clearly visible. This phenomenon is not observed for SiNW-cells because the SiNWs offer a much larger interface area and thus the current density at the Si-SSE interface is much smaller. In the frequency range in which our measurements are made, the capacitive limit is not reached.

In the lithiated state, a semi-circle with a 45° slope at high frequency is observed in both cases at the 1st cycle (Fig. 5cd and Fig. S7). This typical profile has been reported[40] for lithium-ion batteries with a liquid electrolyte, and is attributed to a charge transfer coupled to a diffusion phenomenon associated to the SEI layer. The characteristic frequency of the charge transfer through the SEI is here notably low, around 0.5 Hz, as compared to frequencies above 1 kHz for typical SEI layers in liquid electrolyte cells[41,42]. This frequency is related to the conductivity of the SEI material, following $f_{SEI,Si} = \sigma_{SEI,Si} / 2\pi\varepsilon_0\varepsilon_r$ [42], which indicates that the SEI layer built between silicon and argyrodite has poor conductivity. During cycling, the 45° slope at high frequency is maintained for SiNW-cells in the lithiated state (Fig. S7a). For µSi-cells, the slope at high frequency decreases from 45° to 22.5° after the 5th cycle (Fig. S7b), which is typical of diffusion in a porous material [40,43]. This porosity generation during cycling could be due to the sputtering of the µSi particles as reported earlier[23,44,45]. Note that the situation in SSE is different from liquid electrolyte batteries because there is no new contact between the SSE and the new surfaces created during sputtering. Thus, there is no fresh SEI created, but the sputtering of the particles results in Si particles disconnecting from the rest of the electrode, creating porosity that was not initially present.

The cell impedance associated to the SEI in the lithiated state is twice lower for SiNW- than for µSi-cells, with a total resistance R_{tot} of 24 and 48 Ω.m respectively in the first cycle (Fig. S6d). However, from the irreversible capacity (Fig. 3b) we observed that the mass of SEI formed in SiNW-cells is at least twice that of µSi-cells. Even though part of the SiNW surface is not in contact with the SSE, the contact area between SSE and silicon is orders of magnitude higher in SiNW- than in µSi-cells. Considering that the same current produces the same amount of SEI, we thus conclude that the thickness of SEI on SiNWs is much thinner than the SEI on µSi. Furthermore, the total charge transfer and SEI resistance increases more significantly for µSi-cells, from 48 to 460 Ω.m (i.e. 10 times more) between the 1st and the 15th cycle vs 24 to 170 Ω.m (i.e. 7 times more) for SiNW-cells (Fig. S6d). Thus, even if forming initially a larger mass of SEI in SiNW-cells is detrimental to the overall battery capacity, SiNWs as active material in ASSB advantageously provide a lower and more stable impedance in cycling. This result is consistent with the lower polarization observed on SiNW-cells (Fig. 4a-b).

The greatest differences between the two materials are found in the delithiated state. For SiNW-cells, the profile obtained is close to a 45° line at low frequencies with a lower slope section approaching 22.5° at high frequencies (Fig. S8), which is typical of diffusion in a porous material [40,43]. This porous material corresponds either to the intimate mixture of SiNWs and SSE, the tortuosity of which limits Li^+ diffusion, or to the SiNWs network by itself. Indeed, a large part of the SiNWs are not directly in contact with the SSE but will still lithiate, as shown by the high specific capacity of the electrode, thanks to the diffusion of Li^+ through the porous SiNW network[27]. The resistance obtained at low frequency decreases sharply, up to a factor of 10, compared to the pristine state (Fig. S8), but during cycling, the impedance response does not vary anymore either in terms of slope or frequency.

For µSi-cells in the delithiated state, a semicircle with a 45° slope at high frequency followed by a straight line at 45° is observed, which is characteristic of a charge transfer with diffusion into the SEI and then a diffusion phenomenon into the electrode. The charge transfer part with diffusion in a layer was not visible in the pristine state, as expected from non-lithiated silicon. Indeed, if allowing for relaxation before each impedance measurement, the typical Nyquist profile of a fully delithiated silicon is obtained at the end of delithiation (Fig. S9). Therefore we assume that the µSi is not completely delithiated in the standard C/20 cycling (Fig. 4 and 5). Because of the polarization observed on the galvanostatic curves (Fig. 4b), the potential necessary to completely delithiate the µSi is never reached.

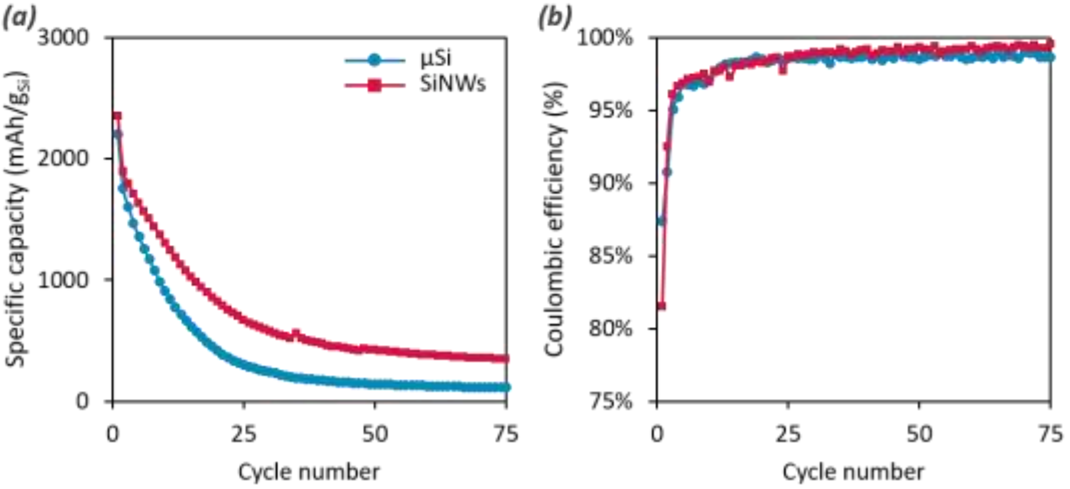

Figure 6: (a) Specific delithiation capacity and (b) Coulombic efficiency of SiNWs/LPSCl/Li-In and µSi/LPSCl/Li-In cells as a function of the number of cycles at a cycling rate of C/20 for the 1st cycle and C/10 for the following cycles, correponding to a current density of 0.82 mA/cm^2 for µSi-cells and 0.52 mA/cm^2 for SiNW-cells. At least three different cells were built for each.

The silicon cycling stability over time was studied by performing long term cycling (Fig. 6). Regardless of the silicon materials used, a drop in capacity at the second cycle is observed, which can be explained by the cycling rate variation. At a cycling rate of C/10 the specific capacity decreases fairly quickly, especially for the µSi-cells, with a capacity retention below 20% at the 20th cycle. At the 50th cycle, the specific capacity is 140 mAh/g_{Si} for µSi-cells and 425 mAh/g_{Si} for SiNW-cells, corresponding to a capacity retention of 7 and 20% respectively. We can assume that this remaining capacity of µSi-cells has no longer any contribution from the silicon, but is rather due to the cycling of the conductive additive and the electrolyte itself, as reported by Trevey *et al*[25]. A cell using 20 wt% VGCF and 80 wt% LPSCl as a composite electrode cycled under the same conditions confirms this hypothesis (Fig. S10). It shows a stable capacity of 0.13 mAh over 100 cycles, whereas the capacities of µSi- and SiNW-cells are respectively 0.1 mAh and 0.28 mAh at the 100th cycle. The capacity is 2.2 times higher for SiNW-cells, showing that some Si lithiation still contributes to the capacity. The CE is lower for the SiNW-cells at the first cycle as seen previously. However, the CE of SiNW-cells is already higher at the 2nd cycle, while at constant cycling at C/20, the CE of SiNW-cells remains lower than that of µSi-cells until the 7th cycle. This difference again highlights the better stability of the SiNWs composite electrode at a cycling rate of C/10 than the µSi-based one.

4. Conclusion

In summary, despite their similar ionic conductivities, LSnPS and LPSCl electrolytes showed a different reactivity in our system with µSi as the active material. The higher reactivity of LSnPS resulted in a faster degradation of performance with only half of the initial capacity at the 5th cycle. LPSCl was therefore chosen to study the influence of silicon size and shape with two different silicon materials, a µSi powder and SiNWs. EDX mapping analysis of the composite powders highlighted the better dispersion of SiNWs and therefore better contact between all the materials in the composite electrode. SiNWs as the active material showed a high initial specific delithiation capacity of 2600 mAh/g_{Si}. µSi provided a slightly higher initial specific delithiation capacity of 2700 mAh/g_{Si}. However, while SiNWs limit the polarization in the electrode and maintain a relatively stable lithiation mechanism during galvanostatic cycling at C/20 rate, a faster degradation of the capacity is observed with µSi. At a cycling rate of C/10, SiNW-cells show also a better stability than the µSi-cells, with silicon still cycling after 100 cycles. In this work, SiNW- and µSi-cells were also studied using EIS, showing that the SEI is thicker in the system minimising the exchange surface (the µSi), which is probably due to a higher surface current density in this system and therefore a higher reactivity. It turns out to be very detrimental during cycling because it leads to a fast loss of capacity. This EIS study also revealed the pulverization of µSi particles during cycling, which is not observed in SiNW-cells. To the best of our knowledge, this work represents the first detailed EIS study of the evolution of the SEI during cycling on an argyrodite / Si system.

Declaration of competing interest

The authors declare that they have no known competing financial interests or personal relationships that could have appeared to influence the work reported in this paper.

Acknowledgement

M. G. acknowledges the financial support of the FOCUS BATTERIES program of CEA.

Author contribution

Martine Grandjean: Investigation, Visualization, Writing – Original draft preparation **Mélanie Pichardo:** Investigation **Yohan Biecher:** Writing – Reviewing and Editing **Cédric Haon:** Writing – Reviewing and Editing, Supervision **Pascale Chenevier:** Resources, Writing – Reviewing and Editing, Supervision

References

(1) Sun, C.; Liu, J.; Gong, Y.; Wilkinson, D. P.; Zhang, J. Recent Advances in All-Solid-State Rechargeable Lithium Batteries. *Nano Energy* **2017**, *33*, 363–386. https://doi.org/10.1016/j.nanoen.2017.01.028.

(2) Shoji, M.; Cheng, E. J.; Kimura, T.; Kanamura, K. Recent Progress for All Solid State Battery Using Sulfide and Oxide Solid Electrolytes. *J. Phys. D: Appl. Phys.* **2019**, *52* (10), 103001. https://doi.org/10.1088/1361-6463/aaf7e2.

(3) Jung, Y. S.; Oh, D. Y.; Nam, Y. J.; Park, K. H. Issues and Challenges for Bulk-Type All-Solid-State Rechargeable Lithium Batteries Using Sulfide Solid Electrolytes. *Israel Journal of Chemistry* **2015**, *55* (5), 472–485. https://doi.org/10.1002/ijch.201400112.

(4) Kerman, K.; Luntz, A.; Viswanathan, V.; Chiang, Y.-M.; Chen, Z. Review—Practical Challenges Hindering the Development of Solid State Li Ion Batteries. *J. Electrochem. Soc.* **2017**, *164* (7), A1731–A1744. https://doi.org/10.1149/2.1571707jes.

(5) Tan, D. H. S.; Wu, E. A.; Nguyen, H.; Chen, Z.; Marple, M. A. T.; Doux, J.-M.; Wang, X.; Yang, H.; Banerjee, A.; Meng, Y. S. Elucidating Reversible Electrochemical Redox of Li_6PS_5Cl Solid Electrolyte. *ACS Energy Lett.* **2019**, *4* (10), 2418–2427. https://doi.org/10.1021/acsenergylett.9b01693.

(6) Sakuda, A.; Takeuchi, T.; Kobayashi, H. Electrode Morphology in All-Solid-State Lithium Secondary Batteries Consisting of LiNi1/3Co1/3Mn1/3O2 and Li2S-P2S5 Solid Electrolytes. *Solid State Ionics* **2016**, *285*, 112–117. https://doi.org/10.1016/j.ssi.2015.09.010.

(7) Wang, X.; He, K.; Li, S.; Zhang, J.; Lu, Y. Realizing High-Performance All-Solid-State Batteries with Sulfide Solid Electrolyte and Silicon Anode: A Review. *Nano Research* **2022**. https://doi.org/10.1007/s12274-022-4526-9.

(8) Dietrich, C.; Weber, D. A.; Sedlmaier, S. J.; Indris, S.; Culver, S. P.; Walter, D.; Janek, J.; Zeier, W. G. Lithium Ion Conductivity in Li_2S–P_2S_5 Glasses – Building Units and Local Structure Evolution during the Crystallization of Superionic Conductors Li_3PS_4, $Li_7P_3S_{11}$ and $Li_4P_2S_7$. *J. Mater. Chem. A* **2017**, *5* (34), 18111–18119. https://doi.org/10.1039/C7TA06067J.

(9) Bron, P.; Johansson, S.; Zick, K.; Roling, B. Li10SnP2S12: An Affordable Lithium Superionic Conductor. *J. Am. Chem. Soc.* **2013**, 4.

(10) Boulineau, S.; Courty, M.; Tarascon, J.-M.; Viallet, V. Mechanochemical Synthesis of Li-Argyrodite Li6PS5X (X=Cl, Br, I) as Sulfur-Based Solid Electrolytes for All Solid State Batteries Application. *Solid State Ionics* **2012**, *221*, 1–5. https://doi.org/10.1016/j.ssi.2012.06.008.

(11) Zheng, B.; Liu, X.; Zhu, J.; Zhao, J.; Zhong, G.; Xiang, Y.; Wang, H.; Zhao, W.; Umeshbabu, E.; Wu, Q.-H.; Huang, J.; Yang, Y. Unraveling (Electro)-Chemical Stability and Interfacial Reactions of Li10SnP2S12 in All-Solid-State Li Batteries. *Nano Energy* **2020**, *67*, 104252. https://doi.org/10.1016/j.nanoen.2019.104252.

(12) Cheng, E. J.; Sharafi, A.; Sakamoto, J. Intergranular Li Metal Propagation through Polycrystalline Li6.25Al0.25La3Zr2O12 Ceramic Electrolyte. *Electrochimica Acta* **2017**, *223*, 85–91. https://doi.org/10.1016/j.electacta.2016.12.018.

(13) Wu, X.; El Kazzi, M.; Villevieille, C. Surface and Morphological Investigation of the Electrode/Electrolyte Properties in an All-Solid-State Battery Using a Li2S-P2S5 Solid Electrolyte. *J Electroceram* **2017**, *38* (2–4), 207–214. https://doi.org/10.1007/s10832-017-0084-z.

(14) Han, F.; Westover, A. S.; Yue, J.; Fan, X.; Wang, F.; Chi, M.; Leonard, D. N.; Dudney, N. J.; Wang, H.; Wang, C. High Electronic Conductivity as the Origin of Lithium Dendrite Formation within Solid Electrolytes. *Nat Energy* **2019**, *4* (3), 187–196. https://doi.org/10.1038/s41560-018-0312-z.

(15) Kasemchainan, J. Critical Stripping Current Leads to Dendrite Formation on Plating in Lithium Anode Solid Electrolyte Cells. *Nature Materials* **2019**, *18*, 8.

(16) Cao, D.; Sun, X.; Li, Y.; Anderson, A.; Lu, W.; Zhu, H. Long-Cycling Sulfide-Based All-Solid-State Batteries Enabled by Electrochemo-Mechanically Stable Electrodes. *Advanced Materials* **2022**, *34* (24), 2200401. https://doi.org/10.1002/adma.202200401.

(17) Cervera, R. B.; Suzuki, N.; Ohnishi, T.; Osada, M.; Mitsuishi, K.; Kambara, T.; Takada, K. High Performance Silicon-Based Anodes in Solid-State Lithium Batteries. *Energy Environ. Sci.* **2014**, *7* (2), 662–666. https://doi.org/10.1039/C3EE43306D.

(18) Ping, W.; Yang, C.; Bao, Y.; Wang, C.; Xie, H.; Hitz, E.; Cheng, J.; Li, T.; Hu, L. A Silicon Anode for Garnet-Based All-Solid-State Batteries: Interfaces and Nanomechanics. *Energy Storage Materials* **2019**, *21*, 246–252. https://doi.org/10.1016/j.ensm.2019.06.024.

(19) Chen, C.; Li, Q.; Li, Y.; Cui, Z.; Guo, X.; Li, H. Sustainable Interfaces between Si Anodes and Garnet Electrolytes for Room-Temperature Solid-State Batteries. *ACS Appl. Mater. Interfaces* **2018**, *10* (2), 2185–2190. https://doi.org/10.1021/acsami.7b16385.

(20) Huo, H.; Sun, J.; chen, C.; Meng, X.; He, M.; Zhao, N.; Guo, X. Flexible Interfaces between Si Anodes and Composite Electrolytes Consisting of Poly(Propylene Carbonates) and Garnets for Solid-State Batteries. *Journal of Power Sources* **2018**, *383*, 150–156. https://doi.org/10.1016/j.jpowsour.2018.02.026.

(21) Ferraresi, G.; El Kazzi, M.; Czornomaz, L.; Tsai, C.-L.; Uhlenbruck, S.; Villevieille, C. Electrochemical Performance of All-Solid-State Li-Ion Batteries Based on Garnet Electrolyte Using Silicon as a Model Electrode. *ACS Energy Lett.* **2018**, *3* (4), 1006–1012. https://doi.org/10.1021/acsenergylett.8b00264.

(22) Li, H. A High Capacity Nano-Si Composite Anode Material for Lithium Rechargeable Batteries. *Electrochem. Solid-State Lett.* **1999**, *2* (11), 547. https://doi.org/10.1149/1.1390899.

(23) Liu, X. H.; Zhong, L.; Huang, S.; Mao, S. X.; Zhu, T.; Huang, J. Y. Size-Dependent Fracture of Silicon Nanoparticles During Lithiation. *ACS Nano* **2012**, *6* (2), 1522–1531. https://doi.org/10.1021/nn204476h.

(24) Cangaz, S.; Hippauf, F.; Reuter, F. S.; Doerfler, S.; Abendroth, T.; Althues, H.; Kaskel, S. Enabling High-Energy Solid-State Batteries with Stable Anode Interphase by the Use of Columnar Silicon Anodes. *Advanced Energy Materials* **2020**, *10* (34), 2001320. https://doi.org/10.1002/aenm.202001320.

(25) Trevey, J. E.; Rason, K. W.; Stoldt, C. R.; Lee, S.-H. Improved Performance of All-Solid-State Lithium-Ion Batteries Using Nanosilicon Active Material with Multiwalled-Carbon-Nanotubes as a Conductive Additive. *Electrochem. Solid-State Lett.* **2010**, *13* (11), A154. https://doi.org/10.1149/1.3479551.

(26) Okuno, R.; Yamamoto, M.; Kato, A.; Takahashi, M. Stable Cyclability Caused by Highly Dispersed Nanoporous Si Composite Anodes with Sulfide-Based Solid Electrolyte. *J. Electrochem. Soc.* **2020**, *167* (14), 140522. https://doi.org/10.1149/1945-7111/abc3ff.

(27) Karuppiah, S.; Keller, C.; Kumar, P.; Jouneau, P.-H.; Aldakov, D.; Ducros, J.-B.; Lapertot, G.; Chenevier, P.; Haon, C. A Scalable Silicon Nanowires-Grown-On-Graphite Composite for High-Energy Lithium Batteries. *ACS Nano* **2020**, *14* (9), 12006–12015. https://doi.org/10.1021/acsnano.0c05198.

(28) Krause, A.; Langklotz, U.; Pohl, D.; Tkacheva, O.; Pohl, D.; Nielsch, K.; Mikolajick, T.; Weber, W. M. Surface Related Differences between Uncoated versus Carbon-Coated Silicon Nanowire Electrodes on Performance in Lithium Ion Batteries. *Journal of Energy Storage* **2020**, *27*, 101052. https://doi.org/10.1016/j.est.2019.101052.

(29) Cui, L.-F.; Yang, Y.; Hsu, C.-M.; Cui, Y. Carbon−Silicon Core−Shell Nanowires as High Capacity Electrode for Lithium Ion Batteries. *Nano Lett.* **2009**, *9* (9), 3370–3374. https://doi.org/10.1021/nl901670t.

(30) Zhang, J.; Fang, S.; Qi, X.; Yu, Z.; Wu, Z.; Yang, J.; Lu, S. Preparation of High-Purity Straight Silicon Nanowires by Molten Salt Electrolysis. *Journal of Energy Chemistry* **2020**, *40*, 171–179. https://doi.org/10.1016/j.jechem.2019.04.014.

(31) Keller, C.; Desrues, A.; Karuppiah, S.; Martin, E.; Alper, J. P.; Boismain, F.; Villevieille, C.; Herlin-Boime, N.; Haon, C.; Chenevier, P. Effect of Size and Shape on Electrochemical Performance of Nano-Silicon-Based Lithium Battery. *Nanomaterials* **2021**, *11* (2), 307. https://doi.org/10.3390/nano11020307.

(32) Burchak, O.; Keller, C.; Lapertot, G.; Salaün, M.; Danet, J.; Chen, Y.; Bendiab, N.; Pépin-Donat, B.; Lombard, C.; Faure-Vincent, J.; Vignon, A.; Aradilla, D.; Reiss, P.; Chenevier, P. Scalable Chemical Synthesis of Doped Silicon Nanowires for Energy Applications. *Nanoscale* **2019**, *11* (46), 22504–22514. https://doi.org/10.1039/C9NR03749G.

(33) Legallais, M.; Nguyen, T. T. T.; Mouis, M.; Salem, B.; Robin, E.; Chenevier, P.; Ternon, C. An Innovative Large Scale Integration of Silicon Nanowire-Based Field Effect Transistors. *Solid State Electron.* **2018**, *143*, 97–102. https://doi.org/10.1016/j.sse.2017.11.008.

(34) Obrovac, M. N.; Chevrier, V. L. Alloy Negative Electrodes for Li-Ion Batteries. *Chem. Rev.* **2014**, *114* (23), 11444–11502. https://doi.org/10.1021/cr500207g.

(35) Santhosha, A. L.; Medenbach, L.; Buchheim, J. R.; Adelhelm, P. The Indium−Lithium Electrode in Solid-State Lithium-Ion Batteries: Phase Formation, Redox Potentials, and Interface Stability. *Batteries & Supercaps* **2019**, *2* (6), 524–529. https://doi.org/10.1002/batt.201800149.

(36) Winter, M.; Novák, P.; Monnier, A. Graphites for Lithium-Ion Cells: The Correlation of the First-Cycle Charge Loss with the Brunauer-Emmett-Teller Surface Area. *J. Electrochem. Soc.* **1998**, *145* (2), 428–436. https://doi.org/10.1149/1.1838281.

(37) Obrovac, M. N.; Krause, L. J. Reversible Cycling of Crystalline Silicon Powder. *J. Electrochem. Soc.* **2007**, *154* (2), A103. https://doi.org/10.1149/1.2402112.

(38) Vivier, V.; Orazem, M. E. Impedance Analysis of Electrochemical Systems. *Chem. Rev.* **2022**, *122* (12), 11131–11168. https://doi.org/10.1021/acs.chemrev.1c00876.

(39) Gruet, D.; Delobel, B.; Sicsic, D.; Lucas, I. T.; Turmine, M.; Vivier, V. Electrochemical Behavior of Pure Graphite Studied with a Powder Microelectrode. *Electrochemistry Communications* **2018**, *95*, 23–27. https://doi.org/10.1016/j.elecom.2018.08.016.

(40) Gruet, D.; Delobel, B.; Sicsic, D.; Lucas, I. T.; Vivier, V. On the Electrochemical Impedance Response of Composite Insertion Electrodes – Toward a Better Understanding of Porous Electrodes. *Electrochimica Acta* **2019**, *295*, 787–800. https://doi.org/10.1016/j.electacta.2018.10.115.

(41) Vadhva, P.; Hu, J.; Johnson, M. J.; Stocker, R.; Braglia, M.; Brett, D. J. L.; Rettie, A. J. E. Electrochemical Impedance Spectroscopy for All-Solid-State Batteries: Theory, Methods and Future Outlook. *ChemElectroChem* **2021**, *8* (11), 1930–1947. https://doi.org/10.1002/celc.202100108.

(42) Desrues, A.; De Vito, E.; Boismain, F.; Alper, J. P.; Haon, C.; Herlin-Boime, N.; Franger, S. Electrochemical and X-Ray Photoelectron Spectroscopic Study of Early SEI Formation and Evolution on Si and Si@C Nanoparticle-Based Electrodes. *Materials* **2022**, *15* (22), 7990. https://doi.org/10.3390/ma15227990.

(43) David Gruet. Modélisation cinétique de la spectroscopie d'impédance électrochimique de cellules Li-ion. Chimie théorique et/ou physique. Sorbonne Université, 2018. Français. NNT : 2018SORUS401. tel-02885982

(44) Jin, Y.; Zhu, B.; Lu, Z.; Liu, N.; Zhu, J. Challenges and Recent Progress in the Development of Si Anodes for Lithium-Ion Battery. *Advanced Energy Materials* **2017**, *7* (23), 1700715. https://doi.org/10.1002/aenm.201700715.

(45) McDowell, M. T.; Lee, S. W.; Nix, W. D.; Cui, Y. 25th Anniversary Article: Understanding the Lithiation of Silicon and Other Alloying Anodes for Lithium-Ion Batteries. *Adv. Mater.* **2013**, *25* (36), 4966–4985. https://doi.org/10.1002/adma.201301795.